

## VU Research Portal

### Crossover between fractal and nonfractal flux penetration in high-temperature superconducting thin films.

Surdeanu, R.; Wijngaarden, R.J.; Dam, B.; Rector, J.H.; Griessen, R.P.; Rossel, C.; Ren, Z.F.; Wang, J.H.

#### **published in**

Physical Review B. Condensed Matter and Materials Physics  
1998

#### **DOI (link to publisher)**

[10.1103/PhysRevB.58.12467](https://doi.org/10.1103/PhysRevB.58.12467)

#### **document version**

Publisher's PDF, also known as Version of record

[Link to publication in VU Research Portal](#)

#### **citation for published version (APA)**

Surdeanu, R., Wijngaarden, R. J., Dam, B., Rector, J. H., Griessen, R. P., Rossel, C., Ren, Z. F., & Wang, J. H. (1998). Crossover between fractal and nonfractal flux penetration in high-temperature superconducting thin films. *Physical Review B. Condensed Matter and Materials Physics*, 58, 12467-12477.  
<https://doi.org/10.1103/PhysRevB.58.12467>

#### **General rights**

Copyright and moral rights for the publications made accessible in the public portal are retained by the authors and/or other copyright owners and it is a condition of accessing publications that users recognise and abide by the legal requirements associated with these rights.

- Users may download and print one copy of any publication from the public portal for the purpose of private study or research.
- You may not further distribute the material or use it for any profit-making activity or commercial gain
- You may freely distribute the URL identifying the publication in the public portal ?

#### **Take down policy**

If you believe that this document breaches copyright please contact us providing details, and we will remove access to the work immediately and investigate your claim.

#### **E-mail address:**

[vuresearchportal.ub@vu.nl](mailto:vuresearchportal.ub@vu.nl)

# Crossover between fractal and nonfractal flux penetration in high-temperature superconducting thin films

R. Surdeanu, R. J. Wijngaarden, B. Dam, J. Rector, and R. Griessen

*Institute COMPAS and Faculty of Physics and Astronomy, Vrije Universiteit, Amsterdam, De Boelelaan 1081, 1081 HV Amsterdam, The Netherlands*

C. Rossel

*IBM Research Division, Zurich Research Laboratory, 8803 Rüschlikon, Switzerland*

Z. F. Ren and J. H. Wang

*Superconductive Materials Laboratory, Department of Chemistry and New York State Institute on Superconductivity, State University of New York at Buffalo, Buffalo, New York 14260-3000*

(Received 28 October 1997; revised manuscript received 20 May 1998)

In this study the role of *anisotropy* on flux penetration in *c*-axis epitaxial  $\text{Ti}_2\text{Ba}_2\text{CuO}_{6+x}$  and  $\text{YBa}_2\text{Cu}_3\text{O}_{7-x}$  films is investigated by magneto-optics. We study thin films of  $\text{Ti}_2\text{Ba}_2\text{CuO}_{6+x}$  on substrates with vicinal angles of  $0^\circ$  (well-oriented),  $0.5^\circ$ ,  $2.5^\circ$ , and  $4^\circ$  and  $\text{YBa}_2\text{Cu}_3\text{O}_{7-x}$  films as a function of chain-conduction-induced anisotropy. A crossover from fractal to nonfractal flux penetration is observed with increasing anisotropy. Numerical simulations of anisotropic flux motion are compared with experiment. [S0163-1829(98)05742-7]

## I. INTRODUCTION

Magneto-optical (MO) investigations of magnetic flux penetration in high- $T_c$  superconducting thin films show often a flux front with a very irregular fractal shape even in high-quality films.<sup>1-9</sup> This behavior is in contrast with the smooth and well-defined flux penetration observed in single crystals<sup>1,2,10-17</sup> and in some thin films.<sup>1,18,19</sup> That the flux penetration in thin films is often more fractal-like than in single crystals is rather surprising since the stability of the flux front should increase for decreasing thickness, and hence be very stable in the thin-film case. From a technical point of view, fractal flux penetration is undesirable in, e.g., thin-film devices since it may lead to increased electrical noise due to the irregular motion of the flux. Although observed before,<sup>1-9</sup> the irregular behavior of the flux front in thin films has not been studied from a fractal point of view. However, a fractal analysis of the superconducting clusters near  $T_c$  was done in  $\text{YBa}_2\text{Cu}_3\text{O}_{7-x}$  films.<sup>20</sup> The notion of *fractal* was introduced by B.B. Mandelbrot<sup>21</sup> in 1967, who showed that it can be a useful concept in studying various phenomena appearing in nature.<sup>22,23</sup> In this paper we study (i) the origin of the fractal behavior and (ii) means to decrease the irregularity of the flux front. In particular, we present a study of the crossover from fractal to nonfractal flux penetration in thin films as a function of anisotropy in the critical current density. This crossover is realized in two ways; (i) by introducing anisotropy in intrinsically isotropic  $\text{Ti}_2\text{Ba}_2\text{CuO}_{6+x}$  films by means of a vicinal (stepped) substrate; (ii) by introducing isotropic behavior in intrinsically anisotropic *ab*-oriented  $\text{YBa}_2\text{Cu}_3\text{O}_{7-x}$  films by means of blocking the chain conduction. To our knowledge, all previous studies<sup>24</sup> on anisotropic *ab*-oriented thin films were done on  $\text{YBa}_2\text{Cu}_3\text{O}_{7-x}$  on vicinal substrates.

The interest in  $\text{Ti}_2\text{Ba}_2\text{CuO}_{6+x}$  films was raised by the

simplicity of their structure: tetragonal symmetry with only one  $\text{CuO}_2$  plane per unit cell and no  $\text{CuO}$  chain.<sup>25-30</sup> This property suggested  $\text{Ti}_2\text{Ba}_2\text{CuO}_{6+x}$  to be an ideal candidate for an unambiguous determination of the pairing symmetry in copper oxide superconductors, as was done in the tricrystal experiment by Tsuei and co-workers.<sup>26,31</sup> Other experiments for determining the pairing symmetry were done by Rossel *et al.*<sup>27</sup> and Willemin *et al.*<sup>32</sup> using a high-sensitivity capacitive torque magnetometer technique on  $\text{Ti}_2\text{Ba}_2\text{CuO}_{6+x}$  thin films. Another reason of interest is the continuously adjustable  $T_c$  over a large range of temperature, from 0 K up to 85 K by varying  $x$ .

This paper is organized as follows: a short description of the high-resolution magneto-optical experimental setup and of the sample preparation procedure is given in Sec. II. Results on  $\text{Ti}_2\text{Ba}_2\text{CuO}_{6+x}$  thin films are presented in Sec. III, beginning with the well-oriented films and increasing the vicinal angle, observing the crossover from isotropic fractal to anisotropic nonfractal behavior. Anisotropy in circular samples is determined by comparison with the simulations discussed in Sec. IV. Guiding of the vortex motion by the vicinal steps is discussed in Sec. V and a comparison with the anisotropic flux penetration in  $\text{YBa}_2\text{Cu}_3\text{O}_{7-x}$  thin films is made in Sec. VI. In Sec. VII the various experimental results are compared with numerical simulations exhibiting also a transition from fractal to nonfractal behavior.

## II. EXPERIMENT AND SAMPLE PREPARATION

Epitaxial  $\text{Ti}_2\text{Ba}_2\text{CuO}_{6+x}$  thin films are made by RF magnetron sputtering, followed by a two-step postdeposition annealing.<sup>25</sup> The sputtering source is prepared by pressing and sintering an intimate mixture of  $\text{Ti}_2\text{O}_3 + 2\text{BaO}_2 + \text{CuO}$  with twice preheating and an intermediate regrounding. The precursor films are deposited by rf magnetron sputtering at

room temperature. The as-deposited films are then annealed in two steps, the last one in flowing argon, in order to get high-temperature superconducting epitaxial films. The  $T_c$  of the samples is about 83 K as determined resistively.

SrTiO<sub>3</sub> platelets of typically  $10 \times 10 \times 1$  mm<sup>3</sup> are used as substrates. The normal to the platelet is either along the (001) direction or at a small angle, which is called the vicinal angle. Films are sputtered on substrates with the following vicinal angles: 0°, 0.5°, 2.5°, and 4°. The patterning into shapes of disks and squares is done using conventional photolithography.

The YBa<sub>2</sub>Cu<sub>3</sub>O<sub>7-x</sub> thin films are grown by pulsed laser deposition (conditions as in Ref. 33) on (001) NdGaO<sub>3</sub> substrates and patterned by standard photolithography. X-ray diffraction shows that the NdGaO<sub>3</sub> substrates are well oriented (0° with an accuracy of 0.1°). In these YBa<sub>2</sub>Cu<sub>3</sub>O<sub>7-x</sub> films, the  $c$  axis is perpendicular to the substrate while the  $a$  and  $b$  axis have the same orientation over the whole film, as verified by Rutherford backscattering and x-ray texture analysis.<sup>34</sup> These films will be denoted henceforth as  $ab$ -oriented YBa<sub>2</sub>Cu<sub>3</sub>O<sub>7-x</sub> films. The chemical composition of the films was investigated with secondary ion mass spectrometry (SIMS).<sup>35</sup>

As indicator for the local magnetic field in the magneto-optical experiments we use Bi-doped YIG films<sup>18</sup> with in-plane anisotropy, which exhibit a large Faraday effect (typically 0.03°/mT) and can be used for a large range of temperatures, from 1.5 K up to 300 K. The magnetic resolution is better than 0.1 mT. The indicator is placed on top of the sample and the assembly is mounted in our home-built cryogenic polarization microscope, which is in the variable temperature insert of an Oxford Instruments 1-T Magnet system. The applied magnetic field is parallel with the  $c$  axis of the sample and perpendicular to the indicator. After the analyzer of the microscope, the spatial variation of the perpendicular component of the local induction  $B_z$  at the sample is given as an intensity pattern. The local field  $H_z$  is determined from the pattern using the calibration  $I = \beta f(H_z^2)$ , where  $I$  is the intensity and  $\beta$  is a proportionality constant. The function  $f$  is determined in a separate calibration experiment, while  $\beta$  can be found by relating the intensity with the field at a certain location in the image where the field is known, e.g., far away from the sample, where the local magnetic field is equal to the applied external field.<sup>36</sup> Images were taken using a liquid-nitrogen-cooled ST-138 CCD Camera (Princeton Instruments).

The temperature of the sample is measured with a calibrated RhFe thermometer. The light used for the magneto-optical experiment causes a heating of the sample of about 1 mK.

The vicinal angle of the substrates and the orientation of the  $a, b$  axis with respect to the edges of the substrates were checked with x-ray Laue diffraction. From the Laue pictures we get two vicinal angles  $\gamma$  and  $\varphi$ , referring to the deviation in two perpendicular planes, and one angle  $\theta$ , which indicates the misorientation of the  $a, b$  axis with respect to the edges of the substrates. Figure 1 depicts the angles, as well as the total vicinal angle  $\delta$ , which can be calculated using the formula

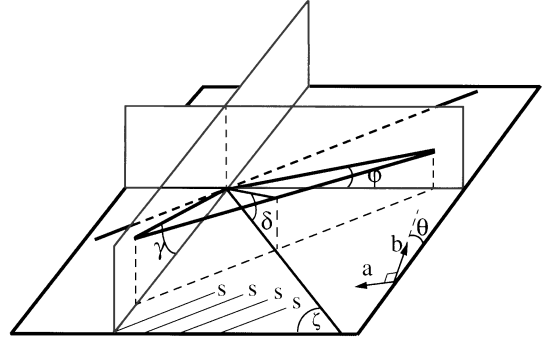


FIG. 1. Angles for the vicinal substrate. The angles  $\varphi$ ,  $\gamma$ , and  $\theta$  are determined from Laue diffraction images and the real vicinal angle  $\delta$  is calculated from  $\varphi$  and  $\gamma$  according to Eq. (1). The lines labeled with  $s$  indicate the direction of the vicinal steps.

$$\delta = \frac{1}{\sqrt{1 + \sin^2 \gamma + \sin^2 \varphi}}, \quad (1)$$

where  $\gamma$  and  $\varphi$  are the vicinal angles from the Laue diffraction image.

### III. RESULTS ON Tl<sub>2</sub>Ba<sub>2</sub>CuO<sub>6+x</sub> THIN FILMS

#### A. 0° vicinal angle (well oriented)

The well-oriented (0° vicinal angle with an accuracy of 0.1°) Tl<sub>2</sub>Ba<sub>2</sub>CuO<sub>6+x</sub> film has a thickness of 500 nm and is patterned into three disk-shaped samples. In the magneto-optical experiment the samples are cooled in zero field to 4.2 K; then the external field is increased. The inset in Fig. 2 presents one of the disk samples at 11 mT. In the MO images, the dark regions are the field-free region, while brighter

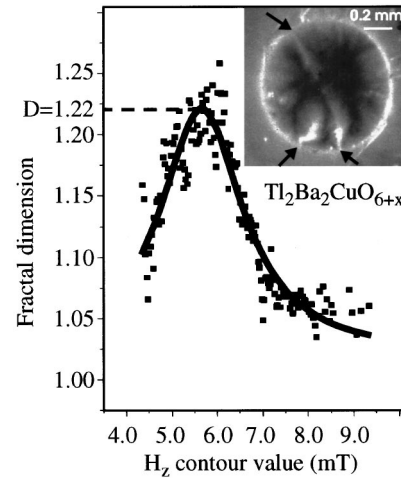


FIG. 2. Fractal dimension (determined as described in Sec. III A) vs  $H_z$  contour value for 0° vicinal angle film, at 11 mT external field,  $T = 4.2$  K. The maximum value 1.22 is taken as the fractal dimension  $D$ ; (inset) Magneto-optical image of one of the disks patterned from a 0° vicinal angle Tl<sub>2</sub>Ba<sub>2</sub>CuO<sub>6+x</sub> thin film, showing fractal flux penetration. The other disks patterned from the same film exhibit very similar patterns. The image is recorded at 4.2 K after zero-field cooling and application of an external field  $\mu_0 H_{ext} = 11$  mT. The arrows point to small defects at the edge of the sample.

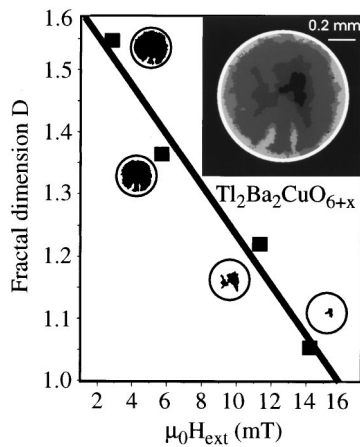


FIG. 3. Fractal dimension vs applied external field for the  $0^\circ$  vicinal angle  $\text{Ti}_2\text{Ba}_2\text{CuO}_{6+\delta}$  film,  $T = 4.2$  K (the line is a guide to the eye). The square symbols represent the calculated fractal dimension  $D$ . The corresponding Meissner regions, as measured magneto-optically, are indicated near the symbols; (inset) Flux fronts (as defined in the text) in the disk patterned from a  $0^\circ$  vicinal angle  $\text{Ti}_2\text{Ba}_2\text{CuO}_{6+\delta}$  film, at several values of the external applied field: 3 mT (inner boundary of light gray area), 5 mT, 11 mT, and 14 mT (inner boundary of dark gray area).  $T = 4.2$  K.

regions correspond to higher local fields. As for the Bean model the vortex density and hence the local field are highest at the sample edge and decrease towards its interior until they vanish: the dark part of the sample is still in the Meissner state. The fractal flux penetration is not only evident from the flux front, but also from the flux density in the region between the sample perimeter and the flux front. This “flux scape” can be characterized by the fractal dimensions of contour lines taken at different values of  $H_z$ . To find the fractal dimension of a contour line, its perimeter is determined using various yardsticks.<sup>22</sup> The perimeter lengths are then plotted as a function of the yardstick values, yielding a nearly straight line in a log-log plot. The slope of this line is by definition the fractal dimension. This slope and its  $1\sigma$  error bar are determined using a least-square fit to a straight line. In our case the yardstick was the pixel size, and we take different yardsticks by reducing the number of pixels in the image. If these fractal dimensions are plotted versus fixed values of the local field  $H_z$ , a Lorentzian curve is obtained. An example at an external field of 11 mT is shown in the graph in Fig. 2. The width of the Lorentzian curve in this particular case is 1 mT. The maximum of this Lorentzian is used below as the fractal dimension  $D$ , while the contour in the image corresponding to the  $H_z$  value at the maximum will be called flux front below.

In the remaining part of this section, we discuss the dependence of the fractal dimension  $D$  for the  $0^\circ$ -sample as a function of external field. The dependence of the fractal dimension on vicinal angle will be discussed in Sec. VII.

The inset in Fig. 3 shows the flux fronts for the same disk patterned on the  $0^\circ$  vicinal angle film. Border lines between regions with different gray values represent the flux fronts at different values of the applied field. The edge of the sample is indicated by the thick white line. Figure 3 presents the plot of  $D$ , calculated for these flux fronts, versus external field. With increasing field, the fractal dimension of the flux front

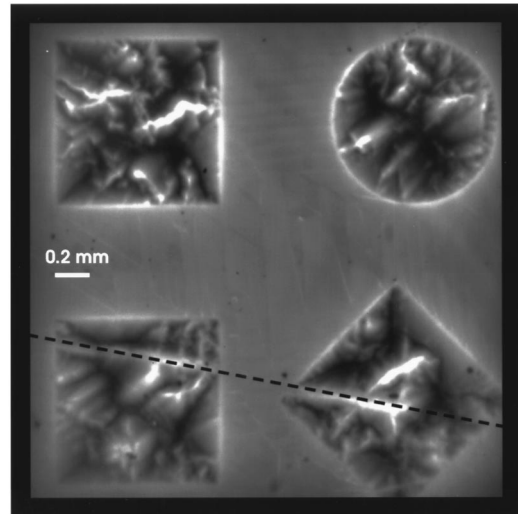


FIG. 4. Magneto-optical image of three squares and one circle patterned from a  $0.5^\circ$  vicinal angle  $\text{Ti}_2\text{Ba}_2\text{CuO}_{6+\delta}$  thin film,  $\mu_0 H_{ext} = 56$  mT,  $T = 4.2$  K. Note that the flux penetration is still irregular although in the disk the pattern is slightly elongated. The black dashed line indicates the only long defect visible under the polarization microscope.

decreases towards  $D = 1$ , the value for nonfractal behavior. The first vortices entering the superconducting sample are guided by randomly distributed weak links; the flux penetration has a strong fractal character. While the flux advances inside the sample, the density of vortices increases and the flux front becomes smoother, with a lower fractal dimension, possibly because the interaction between vortices and weak pinning tends to relax the induction profile.

The irregular penetration as shown in the inset of Fig. 2 is not only due to the fractal penetration process. It is also partly caused by three defects at the sample perimeter (indicated by arrows) that give rise to enhanced penetration of flux. Since there are only three such defects there is not much influence on the fractal dimension. It is important to note that apart from the disturbance by these defects, the overall flux penetration is isotropic, although fractal. Below, samples with anisotropic flux penetration will be discussed.

### B. $0.5^\circ$ vicinal angle

The  $0.5^\circ$  vicinal angle  $\text{Ti}_2\text{Ba}_2\text{CuO}_{6+\delta}$  thin film has a thickness of 500 nm. The film was patterned into a disk, into two squares with the sides oriented parallel to the edges of the substrate, and into one square tilted with respect to the edges at  $45^\circ$ . Figure 4 shows an image taken at 56 mT external field after zero-field cooling to 4.2 K. There are three features that can be observed. (i) The flux penetration is again fractal with a strong influence of defects. Small defects at the edges cause the magnetic flux to penetrate the sample due to enhanced local field.<sup>37</sup> These defects can be seen at the edges of all samples shown. The black dashed line indicates the only long defect visible under a polarization microscope. (ii) The flux front's behavior is the same in all the samples shown, regardless of the shape of the samples. It can be seen that the shape or the position of the sample on the substrate does not influence the fractal-like behavior. (iii) Because of the very high irregularity of the flux penetration,

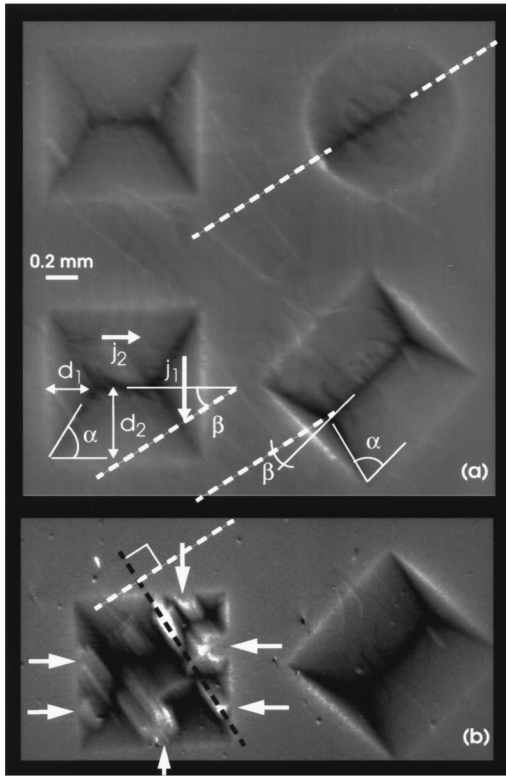


FIG. 5. (a) Magneto-optical image of three squares and one circle patterned from a 2.5° vicinal angle  $\text{Tl}_2\text{Ba}_2\text{CuO}_{6+\delta}$  thin film,  $\mu_0 H_{ext} = 28$  mT,  $T = 4.2$  K. Note that the flux penetration is very regular, if anisotropic. Angles  $\beta$  between the “apparent anisotropy axis” and the “real anisotropy” direction are also indicated. Symbols are explained in the text. (b) Magneto-optical image of the two squares shown in the lower half of Fig. 5(a), after scratching the edges of the lower-left-hand side square at  $\mu_0 H_{ext} = 28$  mT and  $T = 4.2$  K. The arrows indicate the locations where the scratches were made. The difference in contrast between the images of the scratched and unscratched square is due to a different gray scale, which was adapted to show more clearly that the direction of the vortex motion (black dashed line) is perpendicular to the real anisotropy axis (white dashed line).

the determination of the so-called discontinuity lines for the square samples, or of a preferential direction for the superconducting current is hard to make. There can only be a very rough estimate of the critical current,  $j_c$ , anisotropy in this case. However, a close comparison between the flux fronts of the disk samples at 0° and 0.5° shows that the latter is somewhat more elongated (see the insets of Fig. 12), which is an indication of anisotropy of the critical currents.

### C. 2.5° vicinal angle

The 2.5° vicinal angle film has a thickness of 200 nm. We used the same shapes for patterning as for the previous film. The edges of two of the squares are parallel to the edges of the substrate. Figure 5(a) depicts the magneto-optic image at 28 mT on ramping up the field, after a zero-field cooling down to 4.2 K. Clearly, the image is very different from that of the 0.5° vicinal angle film. We consider now the same features of interest as in the previous subsection, but starting with the last two: (iii) the current flow anisotropy and (ii) the shape dependence. The striking difference with the previous

experiment comes from the well-defined anisotropy in the flux penetration. This can be related to the anisotropy in the critical currents. In one direction the magnetic flux penetration is easier, which gives a lower current density in the perpendicular direction. We have to take into account that the current always flows parallel to the edges of the sample. From the continuity equation, for the current flow [the same current flows through the sections defined by  $d_1$  and  $d_2$ , see Fig. 5(a)], we can determine the ratio between the current densities (flowing in the two perpendicular directions parallel to the edges), as being  $j_1/j_2 = \tan \alpha$ , where  $j_1$  and  $j_2$  are the superconducting currents densities flowing in the indicated directions. For the two squares in the left half of Fig. 5(a), the apparent anisotropy value is 1.48, while for the tilted square it is 3.6. This “apparent anisotropy”  $A_{app}$  is dependent upon the orientation of the sample edge with respect to the direction of lowest current density, which we call the anisotropy axis. By contrast, the real value of the anisotropy  $A_{real}$  is defined as the ratio between the maximal and the minimal critical current densities. The anisotropy axis can be determined experimentally by the black line in the disk (the disk does not impose a preferred direction of the flux penetration) and makes an angle  $\beta$  with respect to the sides of the square sample [see Fig. 5(a)]. The smaller the angle  $\beta$ , the larger the apparent anisotropy. From the apparent anisotropy  $A_{app} = j_1/j_2$  the “real anisotropy”  $A_{real}$  can be calculated (see the Appendix) by the formula

$$A_{real} = \sqrt{\frac{\tan^2 \beta - A_{app}^2}{A_{app}^2 \tan^2 \beta - 1}} \quad (2)$$

(Note that we are not in the case described in Ref. 39, Fig. 2(h), where the situation is more complicated due to the fact that the current density that would flow perpendicular to the so-called discontinuity lines exceeds the critical current density for that direction.) Taking the angles  $\alpha$  and  $\beta$  as indicated in Fig. 5(a), we obtain the following anisotropy values:  $A_{real} = 4.8$  for the upright squares, with  $\beta = 33^\circ$  and  $\alpha = 56^\circ$ , and  $A_{real} = 5.0$  for the tilted square, with  $\beta = 11^\circ$  and  $\alpha = 74.5^\circ$ . Clearly there is a very good agreement between these two results: the value of the real anisotropy should be the same regardless of the square taken for calculation. Note that, in contrast to the result of Haage *et al.*<sup>24</sup> on  $\text{YBa}_2\text{Cu}_3\text{O}_{7-x}$  films, the anisotropy of our  $\text{Tl}_2\text{Ba}_2\text{CuO}_{6+x}$  samples is independent upon the external field.

A striking feature that appears in the 2.5° vicinal angle sample is that the effect of defects on the flux front is washed out by the anisotropic flux penetration. The flux front in this case is smooth and uniform, as in the single-crystal case and no fractal behavior is observed by increasing the external applied field from zero. The fractal dimension of the flux front is then  $D \approx 1$ . A possible reason for this behavior will be discussed later.

### D. 4° vicinal angle

In Fig. 6 a typical result is shown for a  $\text{Tl}_2\text{Ba}_2\text{CuO}_{6+x}$  sample of 500 nm thickness with 4° vicinal angle. The image was taken at 28 mT upon increasing field, after a zero-field cooling down to 4.2 K. Magnetic domains in the garnet indicator film are visible as zigzag patterns, especially in

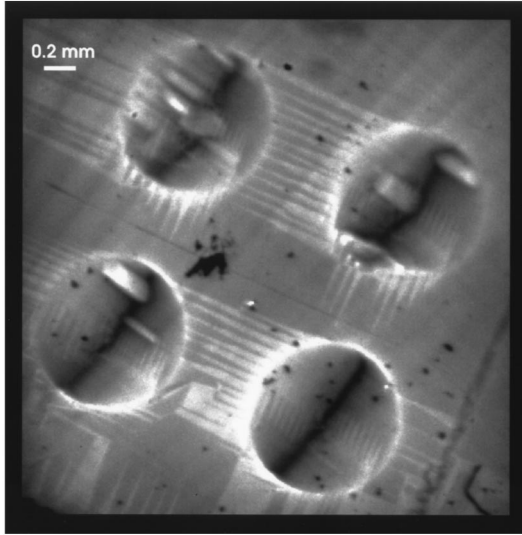


FIG. 6. Magneto-optical image of four circles patterned from a  $4^\circ$  vicinal angle  $\text{Ti}_2\text{Ba}_2\text{CuO}_{6+\delta}$  thin film,  $\mu_0 H_{\text{ext}} = 28$  mT,  $T = 4.2$  K. Note the very high anisotropy in the flux penetration (see also Fig. 7 for comparison). The zigzag patterns in the regions between the samples are magnetic domains in the garnet indicator film, visible due to nonoptimal experimental conditions. Perpendicular to the anisotropy lines are some brighter features that are shadows of small holes in the film.

regions between the samples due to nonoptimal experimental conditions (usually these domains can be made invisible by an appropriate setting of the polarization vector of the incident light with respect to the magnetization vector). The anisotropy lines in the four disk-shaped samples are parallel to each other, indicating clearly that the direction of the real anisotropy is the same for all the samples patterned on the same substrate. In this case, with disks only, we cannot calculate  $A_{\text{real}}$  using Eq. (2). A value of  $A_{\text{real}}$  for this film can be given only by comparison with numerical simulations, to be discussed in the next section. Note that perpendicular to the black anisotropy lines there are some brighter features that are “shadows” of small holes in the films. The holes can be clearly seen with a standard microscope. Although these shadows are present, the anisotropy lines are hardly influenced by them. From these shadows the direction of flux motion during penetration is found to be perpendicular to the anisotropy line, as expected. Clearly the flux penetration in this case, as in the  $2.5^\circ$  case is not fractal and the fractal dimension of the flux front is  $D \approx 1$ .

#### IV. SIMULATIONS OF ANISOTROPIC FLUX PENETRATION

To determine the anisotropy of the critical current from the flux penetration in disk-shaped samples, one cannot use a procedure that exploits the discontinuity lines as we did for Fig. 5(a). In fact flux penetration in anisotropic circular samples is to some extent equivalent to flux penetration in isotropic elliptical samples. The latter case was discussed for the first time by Campbell and Evetts.<sup>40</sup>

To derive an anisotropy value from our experiments we use a numerical simulation model that works as follows. There is a sample area (taken here as a circle) and an outer

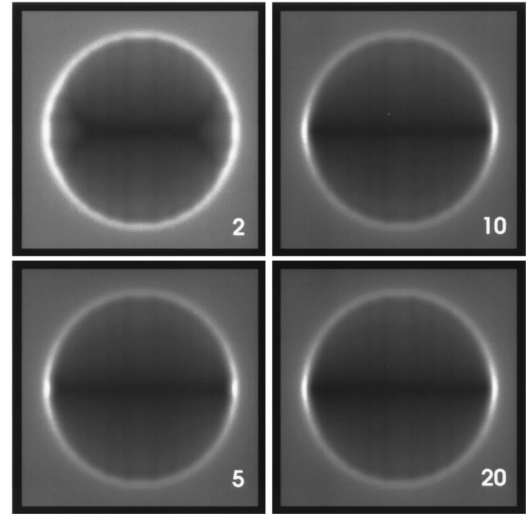


FIG. 7. Simulations for anisotropic disks. Shown is the square of the local field,  $(H_z)^2$ , for disks of the same aspect ratio as in the experiment, to simulate the magneto-optical images. The numbers 2, 5, 10, and 20 indicate the anisotropy value. The Y shape at the ends of the anisotropy line in the case of anisotropy 2 is an artifact due to the square pixels in the simulation. Note that the typical high fields at the edges for the flat samples are nicely reproduced by the simulations.

area, both containing a common square grid of sites. On each site a “height”  $h$  is defined (which will correspond to the vortex density). First this height is set to zero everywhere. Then an iteration starts, where  $h$  in the outer area is increased by 1, followed by relaxation of the inner area. Relaxation is performed by considering each site of the inner area plus a region of one pixel wide around this area. If the value  $h$  for such a site exceeds the value  $h$  of any of its four nondiagonal neighbors by a certain threshold value, then  $h$  of the site under consideration is decreased by 1, while  $h$  of that neighbor is increased by 1 (if there are more such neighbors, one is chosen randomly). This relaxation continues until there is no more change. The whole algorithm ends when there is no inner site left with  $h = 0$ . Anisotropy is introduced in the model by setting the ratio between the horizontal thresholds and vertical thresholds equal to the anisotropy value  $a$ .

The algorithm just described is justified for infinitely thick samples only, where there are only local interactions between vortices. To be able to compare the simulations with our measurements on thin films, we extract the local value of Brandt’s function  $g$  (Ref. 41) from our infinitely thick sample simulation (apart from a constant factor  $g$  it is equal to  $H_z$ ), and then this  $g$  is used to calculate the local magnetic field  $H_z$  using the kernel introduced by Brandt,<sup>41</sup> in this way taking the proper thin-film geometry of the experiment into account.

Results of the simulations for various anisotropy values are shown in Fig. 7. The pictures show the square of the magnetic field,  $(H_z)^2$ , simulating thus the magneto-optical intensity images. Note that the typical high fields at the boundary for the flat samples are nicely reproduced by the simulations. The lines perpendicular to the anisotropy line and the Y profile in the case of anisotropy 2 are due to the square pixels in the calculation.

We verified that the flux profile obtained from a math-

ematical funnel with anisotropic slope (anisotropic Bean model) (Ref. 40) is the same as from our simulation.

From comparison with Fig. 6 we estimate the anisotropy value for the  $4^\circ$  samples to be  $15 \pm 5$ . It is, of course, illustrative to use this same method for the  $2.5^\circ$  sample. Clearly, by comparing the circle in Fig. 5(a) with Fig. 7 for that case a value  $5 \pm 2$  is found, in good agreement with the determination from the discontinuity lines of the squares samples. The values for anisotropy for circular samples, which are found by comparison with the results in Fig. 7, are of course leading to a rather large uncertainty for the anisotropy value as indicated above.

## V. GUIDING OF VORTEX MOTION

We now address the question of why films with higher vicinal angle are less fractal. First of all one might think that films on vicinal substrates are mesoscopically more homogeneous than films on well-oriented substrates. An indication for this phenomenon was obtained by Haage *et al.*<sup>24</sup> for  $\text{YBa}_2\text{Cu}_3\text{O}_{7-x}$  films on  $\text{SrTiO}_3$ . However, in our  $\text{Ti}_2\text{Ba}_2\text{CuO}_{6+x}$  films on  $\text{SrTiO}_3$  an investigation by atomic force microscopy showed that the sample microstructure is not significantly affected by the steps. A possible reason is the postannealing step that is used for the  $\text{Ti}_2\text{Ba}_2\text{CuO}_{6+x}$  films, but not for the  $\text{YBa}_2\text{Cu}_3\text{O}_{7-x}$  films. Secondly, the flux penetration might be influenced by the steps in such a way that fractal behavior is suppressed. Indeed, in this section we show that the vortex movement is guided by the steps present on the vicinal substrates (below we will address the question of whether this is the reason for the disappearance of fractal flux penetration or not). We proceed in two steps. (i) First we compare the direction of the steps in the substrate, as determined by x-ray Laue photography, with the anisotropy axis determined magneto-optically; (ii) then we present an especially designed MO experiment to unambiguously show the guiding of the vortices by vicinal steps.

The geometry is shown in Fig. 1. The true vicinal angle  $\delta$  is the angle formed by the vicinal plane and the horizontal basal plane. These two planes intersect each other on a line that is parallel to the vicinal steps indicated by  $s$  in Fig. 1. The perpendicular line to the steps makes an angle  $\zeta$  with the edges of the substrate. The angle  $\zeta$  can be calculated by

$$\tan\zeta = \frac{\sin\gamma}{\sin\varphi}. \quad (3)$$

For the  $2.5^\circ$  vicinal angle film discussed above,  $\delta = 2.5^\circ$  and  $\zeta = 37.5^\circ$ . Taking into account the angle  $\theta = -3^\circ$ , we find the perpendicular to the vicinal steps at  $34.5^\circ$  with respect to the edge of the substrate. From the magneto-optical measurement it is found that the anisotropy axis makes an angle of  $34.5^\circ$  with respect to the edge of the substrate. Hence, the anisotropy axis (direction of steepest flux gradient) is identified with the perpendicular to the steps in the substrate. Equivalently the direction of easy flux penetration is along the steps. Since in most parts of the sample this direction is crudely perpendicular to the current, this does not yet prove guidance of vortex motion by the steps. For that purpose an other experiment was performed.

On the lower-left-hand square shown in Fig. 5(a) some scratches at the sample edge were made. Figure 5(b) shows the MO image taken in 28 mT external field after a zero-field cooling. The location of the scratches is indicated by arrows. The striking feature is that the vortices entering the superconductor at the defects are not moving perpendicular to the current (which flows parallel to the sample edges). On the contrary, their movement [its direction is indicated by the black dotted line in the Fig. 5(b)] is perpendicular to the real anisotropy axis indicated by the white dotted line. This is a clear indication of guidance of the penetrating flux by the vicinal steps. When applying an external field, fast penetration of vortices at edge defects occurs, followed by the movement along vicinal steps. Note that this flux penetration along the steps is very similar to the flux penetration along twin planes in  $\text{YBa}_2\text{Cu}_3\text{O}_{7-x}$  at low temperature as discussed by Wijngaarden *et al.*<sup>10</sup> This suggests that a similar microscopic mechanism is playing a role. In the left-upper corner we can still observe the  $d$  line, which has the same direction as the  $d$  line in the same square in the “unscratched” experiment [see Fig. 5(a)]. The behavior of the disks with small holes, discussed above and shown in Fig. 6, is completely consistent with these ideas. The white shadows of the defects represent the flux movement from those defects. Clearly, this movement has the same direction as the other vortices (responsible for the induction profile), again along the vicinal steps and perpendicular to the anisotropy axis. One might now be let to believe that the guidance of vortex motion by the vicinal steps causes the disappearance of fractal flux penetration. This possibility will be ruled out in Sec. VII, but it is important to consider first (in the next section) another sample where no such guiding takes place, but which shows nevertheless a transition from fractal to nonfractal behavior as a function of anisotropy.

## VI. RESULTS ON $\text{YBa}_2\text{Cu}_3\text{O}_{7-x}$ THIN FILMS

For comparison with the  $\text{Ti}_2\text{Ba}_2\text{CuO}_{6+x}$  thin films results, we now present MO experiments on  $\text{YBa}_2\text{Cu}_3\text{O}_{7-x}$  epitaxial thin films deposited on well-oriented  $\text{NdGaO}_3$  substrates. The film thickness is only 80 nm to prevent strain in the film.<sup>33,42</sup> The  $\text{YBa}_2\text{Cu}_3\text{O}_{7-x}$  films are grown with the  $c$  axis perpendicular to the substrate and due to crystallographic anisotropy of the substrate surface, the  $a$  and  $b$  axes of the  $\text{YBa}_2\text{Cu}_3\text{O}_{7-x}$  film have the same orientation over the whole substrate surface. This is verified using Rutherford backscattering and x-ray texture analysis.<sup>33</sup> Due to the so-called Cu-O chains of  $\text{YBa}_2\text{Cu}_3\text{O}_{7-x}$ , which run along the  $b$  axis, the electronic structure is anisotropic, leading to, e.g., anisotropy in the resistivity above  $T_c$ .<sup>35,42</sup> Anisotropy of  $j_c$  can thus be expected. However, isotropic  $\text{YBa}_2\text{Cu}_3\text{O}_{7-x}$  films on  $\text{NdGaO}_3$  substrates have been also obtained.<sup>33</sup> A magneto-optical image of a disk patterned from such a film is shown in Fig. 8. The image was taken in 28 mT applied field after a zero-field cooling to 4.2 K. The flux pattern in the sample has an isotropic, fractal character, resembling the result for the  $0^\circ$  vicinal angle (well-oriented)  $\text{Ti}_2\text{Ba}_2\text{CuO}_{6+x}$  sample. We will discuss further results obtained on an  $\text{YBa}_2\text{Cu}_3\text{O}_{7-x}$  film with anisotropy in the resistivity above  $T_c$ , patterned into 2 squares with the edges parallel to the edges of the substrate. Figure 9 shows the MO image taken in 28 mT

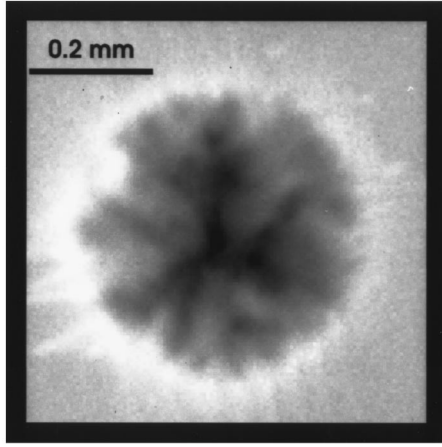


FIG. 8. Magneto-optical image of a circle patterned from an isotropic  $\text{YBa}_2\text{Cu}_3\text{O}_{7-\delta}$  thin film. The image is recorded at  $T = 4.2$  K and an external field  $\mu_0 H_{ext} = 28$  mT.

after a zero-field cooling. Without any vicinal angle of the substrate this sample exhibits an intrinsic anisotropic behavior. Since from other experiments we know that the anisotropy axes are parallel with the edges of the substrate, we can deduce the value for the anisotropy using the same method as in Fig. 5(a). It is found that  $A_{real} = j_a/j_b = 1.3 \pm 0.1$ . This value is much lower compared to  $A_{real} = 5.1$ , found in the  $\text{Tl}_2\text{Ba}_2\text{CuO}_{6+x}$  thin film with  $2.5^\circ$  vicinal angle, where there was a uniform, nonfractal, anisotropic flux pattern. In the  $\text{YBa}_2\text{Cu}_3\text{O}_{7-x}$  experiment, at a closer look, we can observe that at this small anisotropy value, although the flux pattern is reasonably regular, it has still a somewhat fractal behavior.

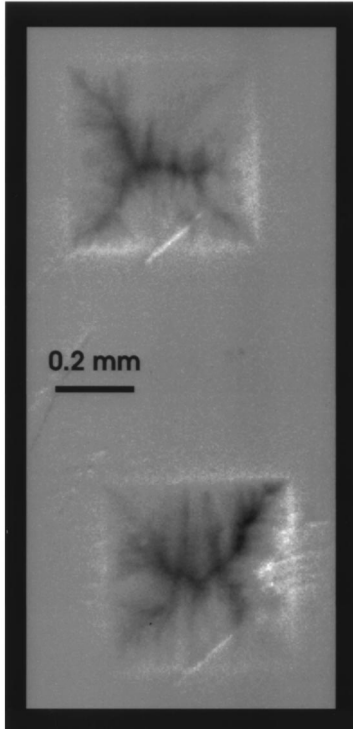


FIG. 9. Magneto-optical image of two squares patterned from an anisotropic  $\text{YBa}_2\text{Cu}_3\text{O}_{7-\delta}$  thin film. The image is recorded at  $T = 4.2$  K and an external field  $\mu_0 H_{ext} = 28$  mT.

As discussed by Dam *et al.*,<sup>35</sup> the anisotropy in resistivity above  $T_c$  depends on the exact growth conditions. SIMS analysis of the Ga content of the films shows no relation between the anisotropy and the purity of the film (the Ga diffuses from the substrate into the  $\text{YBa}_2\text{Cu}_3\text{O}_{7-x}$  film). Nevertheless the amount of Ga in the *chains* may be the key property instead of the total amount of Ga in the film. Alternatively, the oxygenation of the chains may be the dominant factor for the anisotropy. In any case Dam *et al.*<sup>35</sup> derive from a simple Drude model

$$\sqrt{\frac{\rho_a}{\rho_b}} = \frac{j_b}{j_a}. \quad (4)$$

Experimentally we find from resistivity measurements for the film investigated  $\sqrt{\rho_a/\rho_b} = 1.26$ , while the MO experiment gives  $j_b/j_a = 1.3 \pm 0.1$ , in good agreement with Eq. (4). This result is also in good agreement with similar observations on high-quality single crystals by Tamegai *et al.*<sup>43</sup>

Clearly, in the case of  $\text{YBa}_2\text{Cu}_3\text{O}_{7-x}$  the anisotropy is intrinsic, due to an anisotropy in the electronic structure of the superconductor, while in the case of  $\text{Tl}_2\text{Ba}_2\text{CuO}_{6+x}$  the anisotropy is induced by the vicinal steps in the substrate, leading to easy flux penetration along these lines. Immediately two questions arise: (i) Why is the flux penetration at all fractal in the isotropic films? (ii) Why does this fractal behavior disappear as a function of anisotropy? These questions will be addressed in the next section.

## VII. DISCUSSION AND SIMULATIONS OF FRACTAL FLUX PENETRATION

First, we discuss why the flux penetration can be fractal in these films. Flux penetration in high-quality single crystals is very regular and textbooklike.<sup>2</sup> Since the thermal stability of vortex motion is inversely proportion to the sample thickness,<sup>44</sup> one would expect very stable behavior for thin films and regular, nonfractal flux penetration. This is indeed occasionally observed,<sup>1,12,13</sup> but the more common behavior is very irregular. Thermally unstable behavior may occur in thin films only if there are processes that greatly enhance the effect of thermal fluctuations. A possible clue is in the sample microstructure as shown in an Atomic Force Microscopy image for a typical  $\text{YBa}_2\text{Cu}_3\text{O}_{7-x}$  sample in Fig. 10. AFM images obtained for the  $\text{Tl}_2\text{Ba}_2\text{CuO}_{6+x}$  thin films are similar. There are islands separated by trenches with possibly reduced superconducting order parameter and stronger pinning than in the islands. In this scenario, during the flux penetration process, the overall gradient in vortex density is determined by the pinning in the trenches. If one vortex in the trench would depin (by a thermal fluctuation) then due to this motion local heating occurs and the pinning at that point in the trench is reduced, leading to an avalanche process. The analogous vortex picture is shown schematically in Fig. 11.

We just described an amplification mechanism where a fluctuation in the position of one vortex leads to the flow of many vortices, of the order of the number of vortices in one island. This amplification factor is in fact not very high at the fields used, if for the island size 100–200 nm is taken. However, not all trenches are of the same depth (clearly visible in



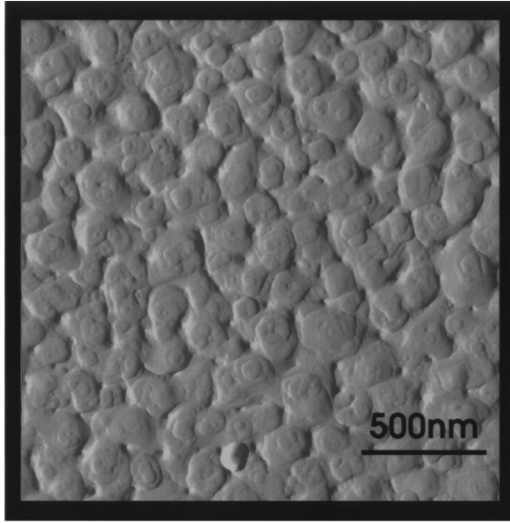


FIG. 10. AFM picture of a typical  $\text{YBa}_2\text{Cu}_3\text{O}_{7-\delta}$  thin film.

Fig. 10) and we believe that this idea is at least qualitatively correct.

Secondly, we discuss the transition from fractal to non-fractal behavior. In Fig. 12 the fractal dimension (determined from the flux scape) of  $\text{Ti}_2\text{Ba}_2\text{CuO}_{6+x}$  films is presented as a function of vicinal angle. For all the vicinal angles the fractal dimension was calculated at the same applied field of 11 mT. Also indicated is the anisotropy in critical current. It is evident that for increasing vicinal angle the anisotropy rapidly increases (note that the  $0^\circ$ ,  $0.5^\circ$ , and  $4^\circ$  samples are 500 nm thick while the  $2.5^\circ$  film is 200 nm thick), and the fractal behavior disappears. To understand the disappearance of fractal penetration note that in the case of very strong anisotropy all vortices (close to the same edge of the sample) move in the same direction and any branching of flux penetration is heavily suppressed. Due to the anisotropy, the number of spatial dimensions for flux penetration is reduced from 2 to 1 leading to nonfractal behavior, although the flux front does

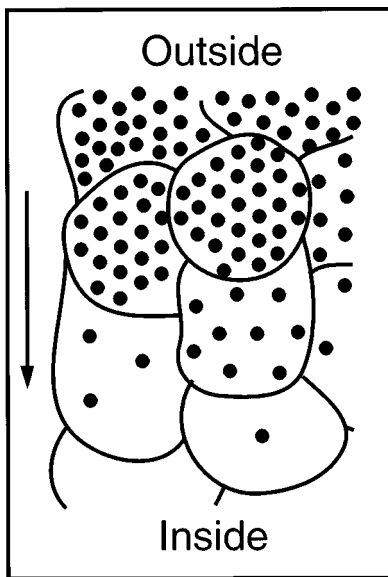


FIG. 11. Schematic picture for vortex motion (see text). The arrow indicates the direction of flux penetration.

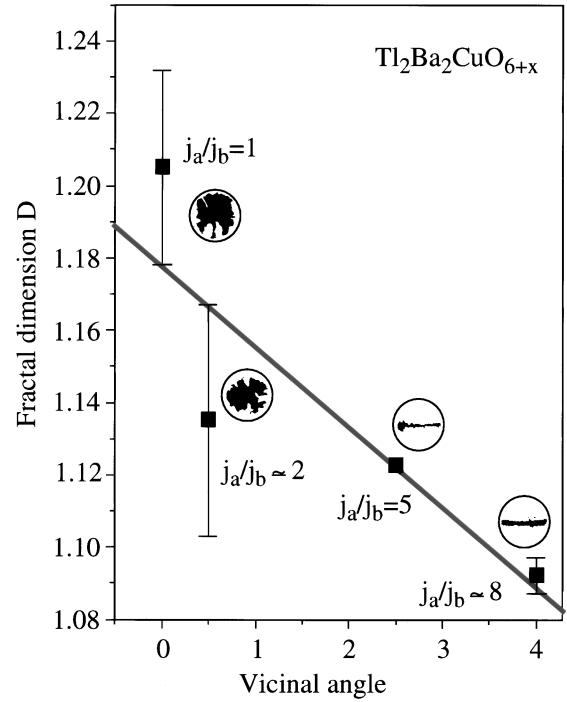


FIG. 12. Fractal dimension vs vicinal angle in  $\text{Ti}_2\text{Ba}_2\text{CuO}_{6+x}$  films. The square symbols represent the calculated fractal dimension  $D$ . The corresponding Meissner regions, as measured magnetooptically, as well as the anisotropy values for the critical current, are indicated near the symbols. For all vicinal angles the fractal dimension was calculated for the applied field of 11 mT. The error bars are found from the least-squares-fit procedure as described in Sec. III A.

not need to be straight. To explore these ideas in more detail, simulations were performed in a similar way to the model discussed above in Sec. IV.

In these simulations the sample area is a square. The sample edge is parallel to the grid of cells. Random pinning is realized by drawing the threshold values  $t$  from the log-normal distribution function

$$P(t) = \sqrt{\frac{\gamma}{\pi}} \frac{e^{-1/4\gamma}}{t_0} \exp\left[-\gamma \left(\ln \frac{t}{t_0}\right)^2\right]; \quad (5)$$

here  $P(t)$  is the probability for the occurrence of the value  $t$ , the width of the distribution is proportional to  $1/\gamma$ , and the center of the distribution is at  $t_0$ . As previously, relaxation is performed by considering each pixel of the inner area plus a region of one pixel wide around this area. If the value  $h$  for such a site exceeds the value  $h$  of any of its four nondiagonal neighbors<sup>45</sup> by a certain threshold value  $t$ , then in the thermally stable case the  $h$  of the site is decreased by 1 and the  $h$  of the neighbor is increased by 1. In the thermally unstable case, both heights are made equal to their average  $h$ . Anisotropy is introduced by taking the thresholds  $t^H$  between pixels that are horizontal neighbors from a different distribution function as the vertical thresholds  $t^V$ . In practice this was done by using one distribution function and dividing all horizontal thresholds by the anisotropy value  $a$ .

Results are shown in Fig. 13, on the right-hand side for the thermally stable case on the left-hand side for the thermally unstable case; also indicated is the fractal dimension of

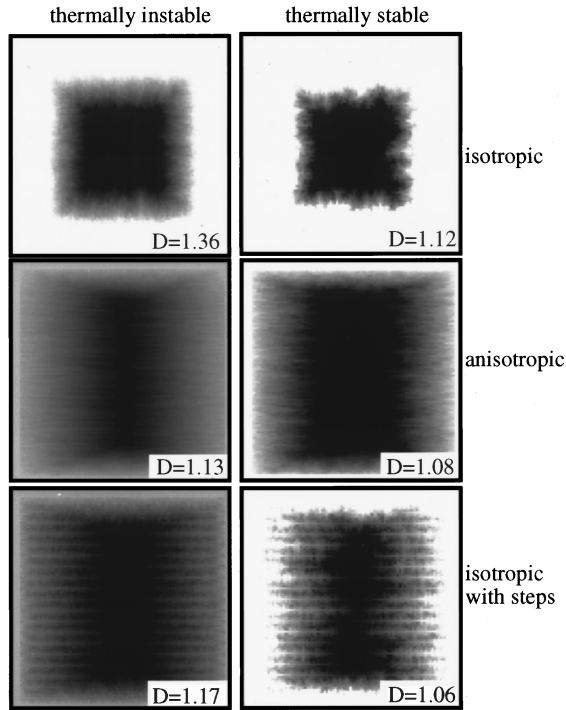


FIG. 13. Simulations with random pinning in the case of thermally stable (right-hand side) and thermally unstable case (left-hand side). The anisotropy used is  $a=5$ , while  $\gamma=1$  (see text). The corresponding fractal dimension is indicated in the figures. We have used the same gray scale for all the images. Due to lower slopes in the lower four figures, these span a smaller contrast range. To allow clear visibility and a fair comparison between the pictures, we have allowed a whiteout to occur in parts of the upper two pictures.

the image as defined above. Clearly, this model leads to fractal flux penetration in the isotropic case. As expected, the fractal dimension in the thermally unstable case is higher than in the thermally stable case. Interestingly, the fractal dimension of the magneto-optical images of the isotropic  $\text{Ti}_2\text{Ba}_2\text{CuO}_{6+x}$  and  $\text{YBa}_2\text{Cu}_3\text{O}_{7-x}$  films are intermediate between these simulation values. In both the thermally stable and the unstable case the flux penetration becomes more regular if anisotropy is introduced (in this case  $a=5$ ). To compare with the  $\text{Ti}_2\text{Ba}_2\text{CuO}_{6+x}$  films, which are isotropic except for the presence of steps along which easy flow of flux is possible, in the bottom frames the isotropic case is shown where along each fifth row of pixels the thresholds were divided by 5. The fractal dimensions were calculated after such coarse graining that the lines were no longer visible, since also in the magneto-optical experiment the individual steps are not visible. It is found that the anisotropic case as well as the isotropic one with steps lead to about the same fractal dimension, which is much lower than that for the isotropic case. In these simulations we find, as in our experiment, a crossover from fractal to nonfractal flux penetration with increasing anisotropy.

Our results may seem contradictory to the theoretical prediction of Gurevich,<sup>46,47</sup> who predicted that anisotropy of critical currents could lead to a fragmentation of magnetic flux. Experimentally it is found that many anisotropic samples<sup>2,10,24</sup> show a regular, although anisotropic, flux pen-

etration. Apparently the conditions for Gurevich's instabilities are not easily met and anisotropy does not induce irregular or fractal flux penetration. However, it does reduce the effective dimensionality for flux penetration and thus suppresses fractal penetration.

## VIII. CONCLUSIONS

Various  $\text{Ti}_2\text{Ba}_2\text{CuO}_{6+x}$  thin films grown on vicinal substrates with angles of  $0^\circ$ ,  $0.5^\circ$ ,  $2.5^\circ$ , and  $4^\circ$ , patterned in shapes of disks, squares and tilted squares were investigated. For increasing vicinal angle a dramatic change in the flux penetration behavior, from a fractal, very irregular one, to a smooth and uniform penetration is found. The crossover is related to the remarkable increase in the critical current anisotropy in the interval  $0.5^\circ - 2.5^\circ$  for the vicinal angle. Clear evidence is presented that, in the case of  $\text{Ti}_2\text{Ba}_2\text{CuO}_{6+x}$  films grown on vicinal substrates, the anisotropy is related to the vicinal steps. A method to calculate the numerical value of the real anisotropy using the MO data for the squares is given. The circular samples are used to determine the real anisotropy axis that we find to be systematic for one substrate. From the direction of this axis and the flux pattern in rectangular samples the real anisotropy value of  $j_c$  is determined.

For comparison with the  $\text{Ti}_2\text{Ba}_2\text{CuO}_{6+x}$  samples,  $\text{YBa}_2\text{Cu}_3\text{O}_{7-x}/\text{NdGaO}_3$  thin films are investigated. Also in these  $\text{YBa}_2\text{Cu}_3\text{O}_{7-x}$  films a crossover from fractal to nonfractal flux penetration is observed. However, due to the lower anisotropy the flux front is not completely regular yet. The anisotropy in the  $\text{YBa}_2\text{Cu}_3\text{O}_{7-x}$  films is due the electronic structure of the sample and is intrinsic. Experimentally the relation between the anisotropy in  $j_c$  and in the resistivity above  $T_c$  is in agreement with a simple Drude model.

In both systems the same transition from fractal to nonfractal behavior is found, although anisotropy is induced by different means. Because of this and of our simulations, we conclude that in general fractal flux penetration can be suppressed by inducing anisotropy. Although anisotropy may not always be desirable, it may be exploited to reduce electric noise in superconducting devices.

## APPENDIX: ANISOTROPIC CRITICAL CURRENT

In this appendix we address the angular dependence of the critical current in the case of anisotropy. Previously, for the case of anisotropy induced by columnar defects Schuster, Kuhn, and Indenbom<sup>38</sup> have given the formula  $j^2 = j_{\min}^2 \cos^2 \alpha + j_{\max}^2 \sin^2 \alpha$ . When  $\alpha$  is interpreted as a polar angle, this formula is incorrect. It is derived from the well-known parametrization for the ellipse  $x = a \cos t$ ,  $y = b \sin t$ , which leads to  $r^2 = a^2 \cos^2 t + b^2 \sin^2 t$ , where the parameter  $t$  is not the polar angle  $\varphi$  (it is easily verified that  $\varphi = \arctan(y/x) = \arctan(b/a \tan t)$ ). A parametrization in terms of the polar angle  $\varphi$  is easily found by substituting  $x = r \cos \varphi$ ,  $y = r \sin \varphi$  in the Cartesian equation  $(x^2/a^2) + (y^2/b^2) = 1$ , where  $r = r(\varphi)$  is the actual radius, which is found to be  $r = [(\cos^2 \varphi/a^2) + (\sin^2 \varphi/b^2)]^{-(1/2)}$ . In anisotropic superconductors, the simple assumption that the angular de-

pendence of the pinning force per length,  $f_p$ , is given by an ellipse, combined with a critical current density given by  $j_c = f_p / \Phi_0$  where  $\Phi_0$  is the flux quantum, leads to the following equation for the critical current as a function of angle:

$$j(\varphi) = \frac{1}{\sqrt{\frac{\cos^2 \varphi}{j_a^2} + \frac{\sin^2 \varphi}{j_b^2}}}. \quad (\text{A1})$$

Finally we note that although the equation for the critical current as a function of angle in Ref. 38 is incorrect, the

formula for the anisotropy [Eq. (1)] in the same paper is correct.

#### ACKNOWLEDGMENTS

This work is part of the research program of the Stichting voor Fundamenteel Onderzoek der Materie (FOM), which is financially supported by the Nederlandse Organisatie voor Wetenschappelijk Onderzoek (NWO). The work performed at the State University of New York at Buffalo (SUNY at Buffalo) was sponsored in part by New York State Energy Research and Development Authority (NYSERDA) and Oak Ridge National Laboratory (ORNL).

- <sup>1</sup>Th. Schuster, H. Kuhn, E.H. Brandt, M.V. Indenbom, M.R. Koblishka, and M. Konczykowski, *Phys. Rev. B* **50**, 16 684 (1994).
- <sup>2</sup>M.R. Koblishka and R.J. Wijngaarden, *Semicond. Sci. Technol.* **8**, 199 (1995).
- <sup>3</sup>M.V. Indenbom, Th. Schuster, M.R. Koblishka, A. Forkl, H. Kronmüller, L.A. Dorosinskii, V.K. Vlasko-Vlasov, A.A. Polyanskii, R.L. Prozorov, and V.I. Nikitenko, *Physica C* **209**, 259 (1993).
- <sup>4</sup>P. Brüll, D. Kirchgässner, and P. Leiderer, *Physica C* **182**, 339 (1991).
- <sup>5</sup>A. Forkl, H.U. Habermeier, B. Leibold, T. Dragon, and H. Kronmüller, *Physica C* **180**, 155 (1991).
- <sup>6</sup>H.U. Habermeier and R. Zaiss, *Cryogenics* **20**, 535 (1980).
- <sup>7</sup>M.R. Koblishka, *Supercond. Sci. Technol.* **9**, 271 (1996).
- <sup>8</sup>Th. Schuster, M.R. Koblishka, H. Kuhn, B. Ludescher, M. Leghissa, M. Lippert, and H. Kronmüller, *Physica C* **196**, 373 (1992).
- <sup>9</sup>Th. Schuster, H. Kuhn, M.R. Koblishka, H. Theuss, H. Kronmüller, M. Leghissa, M. Kraus, and G. Saemann-Ischenko, *Phys. Rev. B* **47**, 373 (1993).
- <sup>10</sup>R.J. Wijngaarden, R. Griessen, J. Fendrich, and W.K. Kwok, *Phys. Rev. B* **55**, 3268 (1997).
- <sup>11</sup>M.V. Indenbom, A. Forkl, B. Ludescher, H. Kronmüller, H.U. Habermeier, B. Leibold, G. D'Anna, T.W. Li, P.H. Kes, and A.A. Menovsky, *Physica C* **226**, 325 (1994).
- <sup>12</sup>Th. Schuster, H. Kuhn, M.V. Indenbom, M. Leghissa, M. Kraus, and M. Konczykowski, *Phys. Rev. B* **51**, 16 358 (1995).
- <sup>13</sup>Th. Schuster, M.V. Indenbom, H. Kuhn, E.H. Brandt, and M. Konczykowski, *Phys. Rev. Lett.* **73**, 1424 (1994).
- <sup>14</sup>R. Potratz, W. Klein, H.U. Habermeier, and H. Kronmüller, *Phys. Status Solidi A* **60**, 417 (1980).
- <sup>15</sup>W. Klein and H. Kronmüller, *Phys. Status Solidi A* **67**, 109 (1987).
- <sup>16</sup>M.V. Indenbom, Th. Schuster, H. Kuhn, H. Kronmüller, T.W. Li, and A.A. Menovsky, *Phys. Rev. B* **51**, 15 484 (1995).
- <sup>17</sup>M. Turchinskaya, D.L. Kaiser, F.W. Gayle, A.J. Shapiro, A. Roytburd, V.K. Vlasko-Vlasov, A.A. Polyanskii, and V.I. Nikitenko, *Physica C* **216**, 205 (1993).
- <sup>18</sup>L.A. Dorosinskii, M.V. Indenbom, V.I. Nikitenko, Yu.A. Ossip'yan, A.A. Polyanskii, and V.K. Vlasko-Vlasov, *Physica C* **203**, 149 (1992).
- <sup>19</sup>M. Baziljevich, *Appl. Phys. Lett.* **69**, 3590 (1996).
- <sup>20</sup>M. Baziljevich, A.V. Bobyl, H. Bratsberg, R. Deltour, M.E. Gaevski, Yu.M. Galperin, V. Gasumyants, T.H. Johansen, I.A. Khrebtov, V.N. Leonov, D.V. Shantsev, and R.A. Suris, *J. Phys. IV* **6**, C3-259 (1996).
- <sup>21</sup>B.B. Mandelbrot, *Science* **155**, 636 (1967).
- <sup>22</sup>B.B. Mandelbrot, *The Fractal Geometry of Nature* (Freeman, New York, 1984).
- <sup>23</sup>A.-L. Barabasi and H.E. Stanley, *Fractal Concepts In Surface Growth* (Cambridge University Press, New York, 1995).
- <sup>24</sup>T. Haage, J.Q. Li, B. Leibold, M. Cardona, J. Zegenhagen, H.-U. Habermeier, A. Forkl, Ch. Jooss, R. Warthmann, and H. Kronmüller, *Solid State Commun.* **99**, 553 (1996); T. Haage, J. Zegenhagen, J.Q. Li, H.-U. Habermeier, M. Cardona, Ch. Jooss, R. Warthmann, A. Forkl, and H. Kronmüller, *Phys. Rev. B* **56**, 8404 (1997).
- <sup>25</sup>C.A. Wang, Z.F. Ren, J.H. Wang, D.K. Petrov, M.J. Naughton, W.Y. Yu, and A. Petrou, *Physica C* **262**, 98 (1996).
- <sup>26</sup>C.C. Tsuei, J.R. Kirtley, M. Rupp, J.Z. Sun, A. Gupta, M.B. Ketchen, C.A. Wang, Z.F. Ren, J.H. Wang, and M. Bhusan, *Science* **271**, 329 (1996).
- <sup>27</sup>C. Rossel, M. Willemin, J. Hofer, H. Keller, Z.F. Ren, and J.H. Wang, *Physica C* **287**, 136 (1997).
- <sup>28</sup>J.D. Jorgensen, O. Chmaissem, J.L. Wagner, W.R. Jensen, B. Dabrowski, D.G. Hinks, and J.F. Mitchell, *Physica C* **282-287**, 97 (1997).
- <sup>29</sup>Z.F. Ren, J.H. Wang, and D.J. Miller, *Appl. Phys. Lett.* **69**, 1798 (1996).
- <sup>30</sup>Z.F. Ren, J.H. Wang, and D.J. Miller, *Appl. Phys. Lett.* **71**, 1706 (1997).
- <sup>31</sup>C.C. Tsuei, J.R. Kirtley, Z.F. Ren, J.H. Wang, H. Raffy, and Z.Z. Li, *Nature (London)* **387**, 481 (1997).
- <sup>32</sup>Willemin, C. Rossel, J. Hofer, H. Keller, Z. F. Ren, and J. H. Wang, *Phys. Rev. B* **57**, 6137 (1998).
- <sup>33</sup>B. Dam, J. Rector, M.F. Chang, S. Kars, D.G. de Groot, and R. Griessen, *Appl. Phys. Lett.* **65**, 1581 (1994).
- <sup>34</sup>J.H. Rector, P. Koster, F. Peerdeman, D.G. de Groot, and B. Dam, *J. Alloys Compd.* **251**, 114 (1997).
- <sup>35</sup>B. Dam, J. Rector, R. Surdeanu, R.J. Wijngaarden, P. Koster, F. Peerdeman, J. van Berkum, D.G. de Groot, and R. Griessen, *Physica C* **282-287**, 665 (1997).
- <sup>36</sup>R.J. Wijngaarden, H.J.W. Spoelder, R. Surdeanu, and R. Griessen, *Phys. Rev. B* **54**, 6742 (1996).
- <sup>37</sup>C.A. Duran, P.L. Gammel, R. Wolfe, V.J. Fratello, D.J. Bishop, J.P. Rice, and D.M. Ginsberg, *Nature (London)* **357**, 474 (1992).
- <sup>38</sup>Th. Schuster, H. Kuhn, and M.V. Indenbom, *Phys. Rev. B* **52**, 15 621 (1995).
- <sup>39</sup>Th. Schuster, M.V. Indenbom, H. Kuhn, H. Kronmüller, M.

- Leghissa, and G. Kreiselmeier, Phys. Rev. B **50**, 9499 (1994).
- <sup>40</sup>A.M. Campbell and J.E. Evetts, Adv. Phys. **21**, 199 (1972).
- <sup>41</sup>E.H. Brandt, Phys. Rev. B **46**, 8628 (1992).
- <sup>42</sup>T. Scherer, P. Marienhoff, R. Herwig, M. Neuhaus, and W. Jutzi, Physica C **197**, 79 (1992).
- <sup>43</sup>T. Tamegai, R. Yamada, T. Yasuhira, and T. Shibauchi, in *Proceedings of the 8th International Workshop on Critical Currents in Superconductors* (IWCC), Kitakyushu, 1996, edited by T. Matsushita and K. Yamafuji (World Scientific, Singapore, 1996), p. 125.
- <sup>44</sup>M. Tinkham, *Introduction to Superconductivity*, 2nd ed. (McGraw-Hill, Inc., 1996), Sec. 5.7.2.
- <sup>45</sup>We found that to be able to generate fractal patterns only four of the closest neighbors must be considered. Otherwise the vortices will move around high thresholds and no fractal behavior results.
- <sup>46</sup>A. Gurevich, Phys. Rev. Lett. **65**, 3197 (1990).
- <sup>47</sup>A. Gurevich, Phys. Rev. B **46**, 3638 (1992).